Extreme Variable-Speed Lubrication Dynamics of Cylinder Block/Valve Plate Interface Based on Neural Network Method

Dingchong LYU[1], Jian FU[1,*], Chao ZHAO[2], Baoyan HU[1], Siyuan CHEN[1], Shoujun ZHAO[3]

[1]School of Mechanical Engineering & Automation, Beihang University, Beijing, China
[2]School of Naval Architecture and Ocean Engineering, Dalian Maritime University, Dalian, Shandong, China
[3]Beijing Institute of Precision Mechatronics and Controls, Beijing, China
E-mail: fujian@buaa.edu.cn

Abstract

High-integrated pump-controlled servo actuators are revolutionizing aerospace hydraulics with superior power-to-weight ratios and dynamic responses. Yet, hydraulic pumps endure extreme operational stresses under high-frequency aerodynamic loads, particularly on the cylinder block and valve plate interface. This critical friction pair governs reliability, efficiency, and lifespan through flow distribution and lubrication. Traditional modeling struggles with multi-physics coupling (turbulent microflows, mixed friction, micro-asperity contact), requiring computationally prohibitive simulations. This study pioneers a physics-informed neural network (PINN) framework to decode dynamic lubrication characteristics under extreme conditions. A high-fidelity numerical model integrates Reynolds-based compressible fluid dynamics and contact mechanics. Physics-constrained PINN training leverages numerical datasets from representative power spectra, with architecture optimized for fluid-solid coupling laws. Experimental validation demonstrates the model's precision in capturing mixed lubrication regimes and transient flow fields under variable speeds/pressures. The PINN achieves way faster computation than numerical methods with < 5% prediction error, enabling real-time analysis. By synergizing first-principles physics with neural operators, this work establishes an intelligent hybrid modeling paradigm for aerospace hydraulic systems, offering transformative solutions for next-generation pump design, condition monitoring, and performance optimization under extreme operational spectra.

Keywords: Electro-hydrostatic actuator, hydrodynamics, numerical simulation, physics-informed neural networks

1 Introduction

Compared to traditional valve-controlled hydraulic systems, highly integrated pump-controlled servo actuators, with their superior power-to-weight ratios and dynamic response characteristics, are increasingly being adopted in aerospace applications [1,2]. In typical aerospace systems such as aircraft flight control surfaces and vector engine servo mechanisms, aerodynamic surfaces are subjected to high-frequency alternating loads. This subjects aerospace servo motor pumps to complex operating conditions involving repeated start-stop cycles, directional reversals, and variable speeds. The high-speed, high-pressure, and dynamically varying operating environments impose significant challenges on internal hydraulic pump components, particularly friction pairs [3–5]. Among these, the cylinder block/port plate pair serves as a critical interface determining the reliability, lifespan, efficiency, and dynamic performance of axial piston pumps. This interface fulfills multiple functions, including flow distribution, load support, lubrication, and sealing. Investigating the operational mechanisms of the cylinder block/port plate pair under high-frequency alternating conditions is essential for enhancing interface performance and represents a vital step toward optimizing the design of high-performance aerospace servo motor pumps [6–8]. The working characteristics of this interface involve complex interactions such as hydrodynamic effects of hydraulic fluid, mixed/boundary friction, micro-elastic deformation of contact surfaces, and thermal deformation. High-fidelity thermo-elasto-hydrodynamic (TEHD) coupling modeling of these phenomena is highly intricate and computationally demanding [9].

Traditional numerical methods rely heavily on mesh quality for accuracy and efficiency. For complex problems, the time required to generate high-quality computational grids often constitutes a substantial portion of the total solution time, significantly increasing computational costs. Artificial neural networks (ANNs) exhibit strong capabilities in approximating arbitrary functions, with deeper networks demonstrating enhanced approximation capacities. Consequently, solving partial differential equations (PDEs) using deep neural networks has emerged as a promising frontier in machine learning, offering an alternative to conventional numerical discretization methods [10]. The application of traditional neural networks in hydraulic system modeling and fault diagnosis dates back to the 1990s, with their core advantage lying in data-driven nonlinear mapping for approximating complex input-output relationships. Karkoub et al. [11] pioneered the use of neural networks in 1999 for predicting the power consumption characteristics of axial piston pumps, marking a breakthrough for data-driven approaches in hydraulics. Subsequent studies expanded their applications: in fault diagnosis, multilayer perceptrons achieved classification of typical failures such as cylinder leakage and port plate wear using vibration spectra and pressure signals [12,13], in performance prediction, Hess et al. [14] employed neural networks to forecast elasto-hydrodynamic lubrication pressures in sliding bearings, while Peric et al. [15] modeled dynamic behaviors of external gear pumps. However, purely data-driven methods face notable limitations: first, their generalization capability heavily depends on the coverage of training data, rendering them inadequate for handling diverse hydraulic operating conditions. Second, the lack of explicit representation of underlying physical mechanisms (e.g., fluid dynamics and contact mechanics) leads to severe reliability degradation in untrained scenarios [14]. Guo et al. [12] emphasized that traditional neural networks for drilling pump fault diagnosis require thousands of labeled datasets, incurring prohibitive experimental costs in practice.

To address these limitations, physics-informed neural networks (PINNs) integrate governing equations into network architectures, enabling synergistic fusion of physical principles and data features. The core innovation lies in embedding physical conservation laws, such as the Navier-Stokes equations and Reynolds lubrication equations [16], as residual constraints within loss functions to form a "physics-regularized" mechanism. Eivazi et al. [17] encoded RANS equations into PINNs, significantly improving turbulent flow prediction efficiency. Ramos et al. [18] further demonstrated their robustness against numerical oscillations in solving microscale Reynolds equations. In hydraulic applications, this hybrid strategy demonstrates unique advantages: Wang et al. [19] and Dong et al. [20] incorporated axial piston pump flow ripple equations as physical constraints, achieving fault identification accuracy at industrially practical levels. Liu et al. [21] developed hierarchical PINNs that synchronously evaluated seal degradation and remaining lifespan by integrating rotor dynamics with sensor data. Yin et al. [22] established a PINNs framework coupling Reynolds equations and contact mechanics to resolve cross-scale challenges in friction pair characterization under seawater lubrication. Ma et al. [23] combined PINNs with proper orthogonal decomposition, enhancing computational efficiency of high-dimensional electro-hydrostatic actuator (EHA) models by two orders of magnitude. Exploring the application of PINNs to solve complex dynamic characteristics of servo motor pump cylinder block/port plate pairs under representative power spectra constitutes a novel and compelling research direction.

This study adopts PINNs to predict dynamic lubrication characteristics of cylinder block/valve plate interfaces under high-frequency conditions. The model integrates the Reynolds equation and contact mechanics into PINNs and is validated with high-fidelity data. It accurately predicts oil film pressure and friction losses, supporting intelligent design of aerospace hydraulic pumps.

2 Preliminaries

The framework integrates hydrodynamic theory, mixed friction characterization under variable speeds, and PINNs embedding conservation laws and experimental data to predict lubricating behavior on the cylinder block/valve plate interface.

2.1 Numerical characterization of dynamic lubrication characteristics

The interface governs lubrication and friction in axial piston pumps via hydrodynamic effects (modeled by Reynolds equations) and solid-contact interactions. The cylinder block's tilt generates a wedge-shaped oil film, producing hydrodynamic pressure to reduce friction. However, transient mixed lubrication arises under variable loads/speeds, requiring simultaneous characterization of fluid-film dynamics (pressure distribution, viscosity effects) and asperity contact forces (boundary friction, wear mechanisms). Geometric parameters like tilt angle and film thickness critically influence regime transitions between hydrodynamic and boundary lubrication.

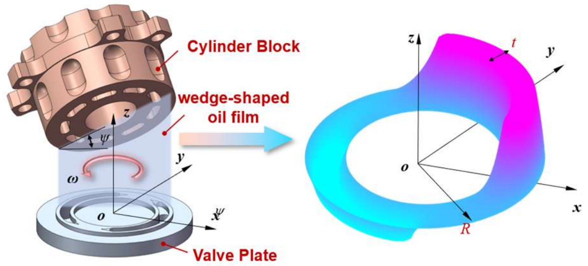

Figure1: Schematic diagram of cylinder block and valve plate pair.

To balance accuracy and computational efficiency, key assumptions streamline the Reynolds equation: (1) Neglect gravity, electromagnetic forces, and fluid inertia, (2) Assume constant viscosity, no wall slip, and isothermal conditions, (3) Approximate circumferential flow as translational motion. These simplifications focus on the dominant factors, such as film thickness dynamics and pressure gradients, while maintaining the predictive capability for mixed lubrication behavior. The reduced model enables efficient analysis of transient friction and lubrication characteristics under variable-speed conditions.

2.2 Transition of mixed lubrication states under variable-speed conditions

In aerospace applications, the inability to sustain hydrodynamic lubrication under rapid speed transitions exacerbates surface interactions, rendering complete fluid lubrication models inadequate. The friction behavior of distribution pairs in high-integrated servo actuators cannot be characterized solely by low-speed regimes or static coefficients. Instead, a dynamic adaptation of the Stribeck framework is essential to map friction transitions across ultra-wide speed spectra (-20,000~20,000 rpm) and capture transient mixed lubrication effects. This adaptation enables precise modeling of friction losses and wear mechanisms in pump-controlled actuators, addressing the unique demands of aerospace systems where reliability and precision are mission-critical.

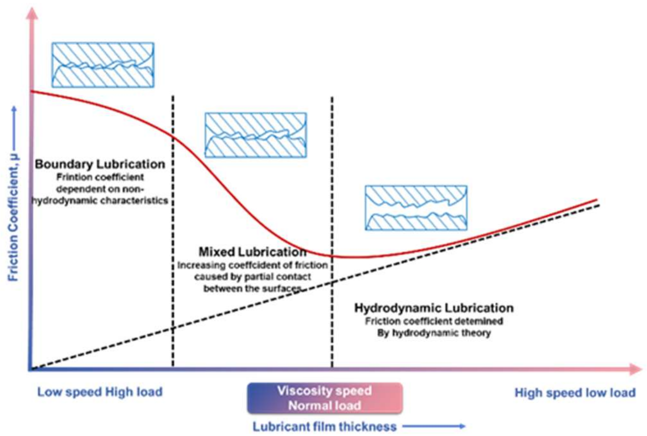

Figure2: Stribeck curve diagram.

2.3 Physics informed neural network prediction

Unlike purely data-driven methods, PINNs synthesize measurement signals and physical residuals through dual loss functions. This capability enables reliable extrapolation in aerospace applications, such as simulating hydraulic pump component behaviors under extreme variable-speed conditions, where experimental data acquisition is costly or impractical. Their interpretable outputs, such as transient pressure fields in dynamic lubrication, bridge theoretical insights with real-world performance validation while maintaining computational efficiency.

Numerical challenges persist in modeling cylinder block/valve plate pairs due to fluid-solid coupling under transient lubrication. Traditional methods (e.g., Runge-Kutta, FEA) suffer from high computational costs and poor convergence under wide-speed ranges, exacerbated by nonlinear hydrodynamic-contact interactions during rapid speed transitions.

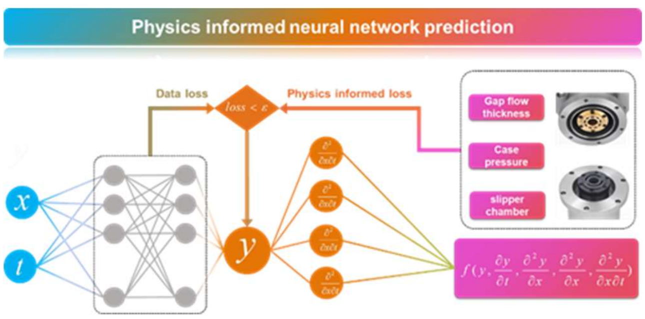

Figure3: Schematic diagram of PINN model.

Implementation trains PINNs using theoretical numerical solutions as ground truth. Inputs include spatiotemporal coordinates (e.g., φ, λ) and operational parameters (e.g., ω, ψ), while outputs predict pressure fields. The loss function integrates PDE residuals, periodicity, and boundary constraints, enabling millisecond-level inference for real-time aerospace mixed lubrication analysis post-training.

3 Neural network design

The construction of PINNs is fundamentally based on governing physical equations. By embedding physical laws as intrinsic constraints, PINNs can significantly reduce the costs associated with data acquisition and storage, demonstrating distinct advantages in addressing complex physical systems.

A Multilayer Perceptron (MLP) with hierarchically structured neurons is employed to execute mathematical operations. Loss functions are formulated based on the residuals derived from the mixed lubrication model of the cylinder block/valve plate interface. Through iterative training, a fully differentiable surrogate model is obtained, whose outputs are differentiable with respect to the inputs. This capability allows for seamless integration with traditional numerical methods while preserving the inherent benefits of neural networks. Fig. 4 [18] illustrates the overall structure of the hybrid lubrication characteristics prediction framework for the cylinder block/valve plate interface based on PINNs.

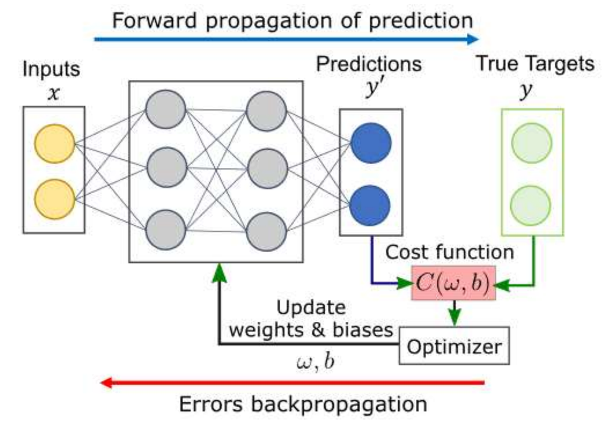

Figure4: Overall structure of the prediction framework. [18]

3.1 Governing equations related to fluid dynamics

In the realm of theoretical research, the characteristics of complete fluid-film lubrication and complete contact friction have been extensively explored and are relatively well-established. However, under the unique aerospace operating conditions pertinent to this study, the characterization equations for the lubrication and friction properties of the friction pair interface remain a subject of ongoing discussion.

3.1.1 Hydrodynamic lubrication characterization

The formulation of dimensionless equations plays a crucial role in streamlining the representation of governing fluid dynamics equations. It not only standardizes the relationships between variables but also minimizes the influence of unit scaling. By reducing variables to a common order of magnitude, the dimensionless form ensures that numerical values remain within a computationally feasible range, avoiding extremes that could compromise simulation accuracy.

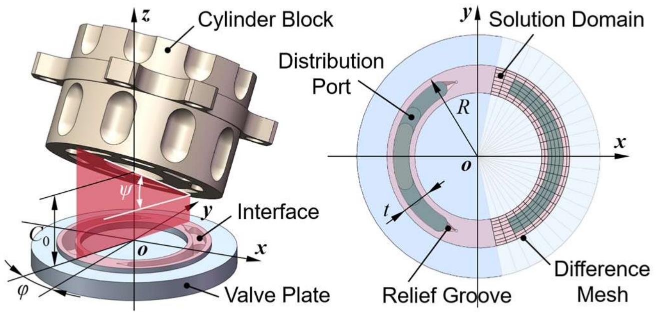

Figure5: Geometry structure of the interface. [8]

In this study, the dimensionless Reynolds equation is employed to characterize the lubrication behavior at the cylinder block/valve plate friction pair, a critical interface in the performance of highly integrated pump-controlled servo actuators. This equation is expressed as follows:

$$\frac{\partial}{\partial\varphi}\left(PH^3\frac{\partial P}{\partial\varphi}\right)+\frac{\partial}{\partial\lambda}\left(PH^3\frac{\partial P}{\partial\lambda}\right)=\Lambda\frac{\partial(PH)}{\partial\varphi}+2\Lambda\frac{\partial(PH)}{\partial T} \quad (1)$$

$$\Lambda=\frac{6\mu\omega}{P_a}\left(\frac{R}{C_0}\right)^2 \quad (2)$$

Where φ and λ denote the dimensionless circumferential and radial coordinates, respectively. T is the dimensionless operating time. P and H represent the dimensionless oil pressure and oil film thickness, respectively. Λ denotes the compressibility number. The tilting angle ψ of the cylinder block and the initial oil film thickness C_0 are incorporated into the characterization of H for the bidirectional coupling solution with rotor dynamics. The force balance analysis of the cylinder block assembly is described in [8].

$$H=\frac{C_0+R\sin\psi\cos(\varphi+\varphi_0)}{R} \quad (3)$$

C_0 is primarily influenced by the oil pressure P, the spring preload force F_{sp}, and the external force exerted by the cylinder block assembly.

3.1.2 Contact friction characterization

The frictional stress in the contact region of the friction pair can be characterized using Hertzian elastic contact theory. Although the contact surface between the cylinder block and valve plate is planar, due to the tilting behavior of the cylinder block, the contact region can be approximated as the interaction between a flat surface and a point (spherical) contact. When a sphere and a flat surface are in contact, the Hertzian stress is expressed as follows:

$$\sigma_{\max}=\sqrt[3]{\frac{6}{\pi^3}\frac{1}{R^2}\left(\frac{N}{\frac{1-\mu_1^2}{E_1}+\frac{1-\mu_2^2}{E_2}}\right)} \quad (4)$$

$$R=\frac{\left(\dot{x}^2+\dot{y}^2\right)^{\frac{3}{2}}}{\dot{x}\ddot{y}-\dot{y}\ddot{x}} \quad (5)$$

Where $\sigma_{\max}$ represents the maximum contact stress, a denotes the contact width, N is the external load, R is the radii of the contacting cylinder, E_1 and E_2 are the Young's moduli, and μ_1 and μ_2 are the Poisson's ratios of the two contacting cylinders.

3.1.3 Integration of contact/non-contact region

In the mixed/boundary friction state, viscous friction dominates in the non-contact region, while coulomb friction prevails in the contact region. Both frictional forces are influenced by the pressure P. The relationship between the two types of frictional torques and the clamping force P is expressed by eq. (6) and (7).

The distribution ratio coefficient ξ between the two types of friction was defined as a specific function to fit the experimental curves in our previous study, as shown in fig. 7.

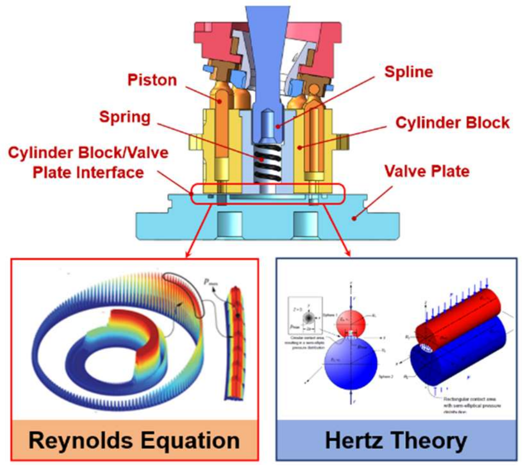

Figure6: Fluid dynamics modeling architecture.

$$T_m=T_v(P)+T_c(P)$$
$$P=P_v+P_c=(1+\xi)P_v \quad (6)$$

$$T_v=P_aR^2C_0\int_{\frac{R-t}{R}}^{1}\int_0^{2\pi}\left(\frac{\Lambda}{6}\frac{1}{H}-\frac{H}{2}\frac{\partial P_v}{\partial\varphi}\right)\mathrm{d}\varphi\mathrm{d}\lambda \quad (7)$$

T_m, T_v, and T_c denote the torques corresponding to mixed friction, viscous friction, and Coulomb friction, respectively. P_v and P_c represent the pressures assigned to viscous and Coulomb friction, respectively.

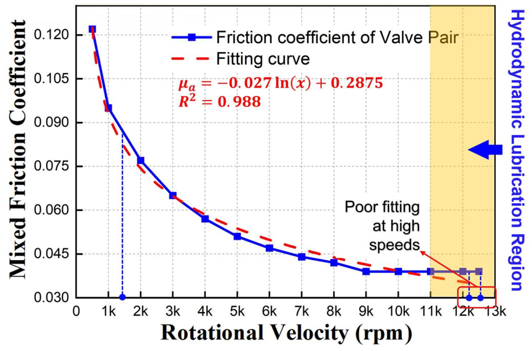

Figure7: Experimental determination of the distribution ratio coefficient ξ.

Table1: *Comparison of circumferential periodicity condition treatments.*

Model Type	Circumferential Periodicity Solution Strategy	Approaches	Key Expressions
Numerical model	Modify the configurations of second-order difference coefficient matrices $D_{\varphi\varphi}$ and $D_{\lambda\lambda}$, incorporating the node values (u_1, u_{X-1}) into each other's difference stencils.	Constructing lost functions	$\left.\frac{\partial^2 u}{\partial \varphi^2}\right\|_{i=1,j} = \frac{u_{X-1,j} - 2u_{1,j} + u_{2,j}}{h_\varphi^2}$
PINN model	Ensure the initial value $p(\varphi = 0, \lambda)$ and terminal value $p(\varphi = 2\pi, \lambda)$ of the pressure distribution remain equal in the circumferential coordinate φ.	Modifying difference matrix	$L_{cir} = \frac{1}{N_{cir}} \sum_{i=1}^{N_{cir}} \left(u_n(\varphi_1) - u_n(\varphi_X)\right)^2$

3.2 Boundary conditions and circularity condition

The equation used to characterize the mixed lubrication characteristics of the cylinder block/valve plate interface serves as the fundamental theoretical basis for PINNs. In addition to satisfying this equation, it is also necessary to consider the geometric structure of the frictional pair's working interface, pressure boundary conditions, and the distribution of contact and non-contact regions.

3.2.1 Circumferential periodicity condition

The working region is an annular zone containing two kidney-shaped grooves. A dimensionless numerical solution method truncates this annular region and approximates it as a rectangular solution domain to facilitate solving via difference matrix operations [8]. Consequently, the neural network model must first satisfy the circumferential periodicity condition of the solution domain. Specifically, in the circumferential coordinate φ direction, the initial value $p(\varphi = 0, \lambda)$ and terminal value $p(\varphi = 2\pi, \lambda)$ of the pressure distribution must remain equal at all times [18], as shown in eq. (8):

$$p(\varphi = 0, \lambda) = p(\varphi = 2\pi, \lambda) \tag{8}$$

It is worth noting that the issue of circumferential periodicity conditions also arises during numerical solution procedures. However, circumferential periodicity can be directly enforced by modifying the configuration of difference matrices without explicitly setting boundary conditions. The fundamental form of the elliptic partial differential equation can be expressed as follows:

$$-c_{ij}\left(\frac{u_{i,j-1} - 2u_{ij} + u_{i,j+1}}{h_\varphi^2} + \frac{u_{i-1,j} - 2u_{ij} + u_{i+1,j}}{h_\lambda^2}\right) + a_{ij}u_{ij} = f_{ij} \tag{9}$$

$$\left[-Diag_c\left(D_{\varphi\varphi} + D_{\lambda\lambda}\right) + Diag_a\right]u = Diag_f \tag{10}$$

Where c, a and f are coefficient values of the elliptic partial differential equation, distributed in main diagonal matrix forms denoted as $Diag_c$, $Diag_a$ and $Diag_f$ are the column vectors of the unknown function values, while h_φ and h_λ represent the unit lengths in the circumferential and radial directions, respectively. The product vectors of matrices $D_{\varphi\varphi}$ and $D_{\lambda\lambda}$ with the column vector u correspond to the second-order partial derivative column vectors of u in the circumferential and radial directions.

Since the column vector u is arranged according to the row-wise node distribution of the rectangular solution domain, the matrix configurations of $D_{\varphi\varphi}$ and $D_{\lambda\lambda}$ can be directly formulated without considering circumferential periodicity. Taking $D_{\varphi\varphi}$ as an example, as shown in eq. (11):

$$D_{\varphi\varphi} = h_\varphi^{-2}\begin{bmatrix} -2 & 1 & & \\ 1 & \ddots & \ddots & \\ & \ddots & \ddots & 1 \\ & & 1 & -2 \end{bmatrix}, N \times N \tag{11}$$

Where N is the total number of nodes in the solution domain. When incorporating circumferential periodicity, the function values of the first node in each row and the second-to-last node in the same row are mutually assigned as difference elements, expressed as:

$$\left.\frac{\partial^2 u}{\partial \varphi^2}\right|_{i=1,j} = \frac{u_{X-1,j} - 2u_{1,j} + u_{2,j}}{h_\varphi^2} \tag{12}$$

$$\left.\frac{\partial^2 u}{\partial \varphi^2}\right|_{X-1,j} = \frac{u_{X-2,j} - 2u_{X-1,j} + u_{1,j}}{h_\varphi^2} \tag{13}$$

Where X is the number of row nodes and Y is the number of column nodes. Based on the above expressions, the form of $D_{\varphi\varphi}$ can be transformed into the structure shown in eq. (14), where the left side is a $Y\times Y$ identity matrix and the right side is an $(X\text{-}1)\times(X\text{-}1)$ matrix. The same logic applies to $D_{\lambda\lambda}$. This matrix transformation ensures circumferential periodicity mathematically, effectively converting the rectangular solution domain back to a ring-shaped region physically. A comparison between the numerical method and neural network algorithm for handling circumferential periodicity conditions is summarized in Table 1.

$$D_{\varphi\varphi} = h_\varphi^{-2}\begin{bmatrix} 1 & & & \\ & \ddots & & \\ & & \ddots & \\ & & & 1 \end{bmatrix} \otimes \begin{bmatrix} -2 & 1 & & 1 \\ 1 & \ddots & \ddots & \\ & \ddots & \ddots & 1 \\ 1 & & 1 & -2 \end{bmatrix} \tag{14}$$

3.2.2 Pressure boundary conditions

The setting of pressure boundary conditions. In the two kidney-shaped groove regions, one side corresponds to the high-pressure zone (suction port), where the pressure remains consistent with the load-end pressure p_{out}, while the other side corresponds to the low-pressure zone (discharge port), where the pressure aligns with the system pressure p_{in}. Additionally, the inner and outer boundaries of the annular solution domain maintain consistency with the pressure within the hydraulic pump chamber p_c, as shown below:

$$p(\varphi, \lambda \in R_{in}) = p_{in} \tag{15}$$

$$p(\varphi, \lambda \in R_{out}) = p_{out} \tag{16}$$

$$p(\varphi, \lambda = r_1) = p(\varphi, \lambda = r_2) = p_c \tag{17}$$

Where R_{in} and R_{out} are subsets defining the ranges of the suction and discharge port kidney-shaped groove regions, respectively, and r_1 and r_2 represent the inner and outer radii of the solution domain.

3.2.3 Boundary conditions for contact/non-contact region

Under wide-range variable-speed and variable-pressure operating conditions, the cylinder block/valve plate interface struggles to form a stable oil film for support, resulting in a complex lubrication/friction state where contact and non-contact zones coexist. Neither a standalone hydrodynamic model nor a contact mechanics model is sufficient to describe such intricate lubrication characteristics.

In our prior research, to couple hydrodynamic and contact mechanics models for characterizing mixed/boundary lubrication states, we utilized friction test data from the cylinder block/valve plate interface to generate mixed friction coefficient-rotational speed curves. The proportion of viscous friction to contact friction was determined based on friction coefficients obtained under specific test conditions [8]. Consequently, mixed friction/lubrication behavior was primarily characterized by a proportionality factor ξ, as shown in eq. (18). However, this proportionality factor holds purely mathematical significance—it neither physically explains the mechanism of mixed friction/lubrication nor exhibits general applicability.

$$F_{\text{t}} = F_{\text{v}}(p) + F_{\text{c}}(p) = (1+\xi)F_{\text{v}}(p) \tag{18}$$

Where F_{t}, F_{v}, and F_{c} represent the residual clamping force, hydrodynamic support force, and contact support force, respectively.

To address these limitations, we revisited the coupling methodology of the two friction models. By observing wear patterns on the friction pair specimen surfaces under specific speed/pressure conditions, we determined the distribution of contact/non-contact zones. This distribution was then used to define the solution domains for the two friction models, and mixed friction coefficients were solved based on mechanical equilibrium equations, as illustrated in fig. 8. Detailed implementation steps are provided in Chapter 4. The governing equations are as follows:

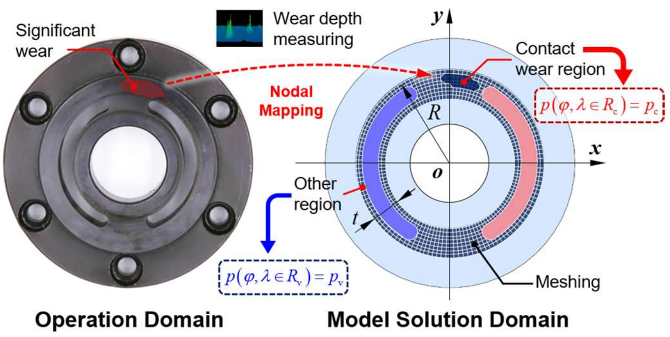

Figure8: Characterizations of contact/non-contact region.

$$p(\varphi,\lambda \in R_{\text{v}}) = p_{\text{v}} \tag{19}$$

$$p(\varphi,\lambda \in R_{\text{c}}) = p_{\text{c}} \tag{20}$$

$$F_{\text{t}} = F_{\text{v}}(p) + F_{\text{c}}(p) = \iint_{\varphi,\lambda \in R_{\text{v}}} p_{\text{v}} \mathrm{d}\varphi \mathrm{d}\lambda + \iint_{\varphi,\lambda \in R_{\text{c}}} p_{\text{c}} \mathrm{d}\varphi \mathrm{d}\lambda \tag{21}$$

Where R_{v} and R_{c} are subsets defining the experimentally observed non-contact and contact zones, respectively, and p_{v} and p_{c} denote the pressure distributions calculated by hydrodynamic and contact mechanics theoretical models.

3.3 Network loss function

Based on the mixed lubrication model equations for the cylinder block/valve plate pair interface and the boundary/circumferential conditions outlined in Section 3.2, the loss function for PINNs can be constructed as the sum of residuals from the governing differential equations, circumferential periodicity errors, pressure boundary condition errors, and contact zone distribution errors, as shown in eq. (22)~(26). By minimizing the mean squared error (MSE), measured signals are set as learning objectives for training the neural network.

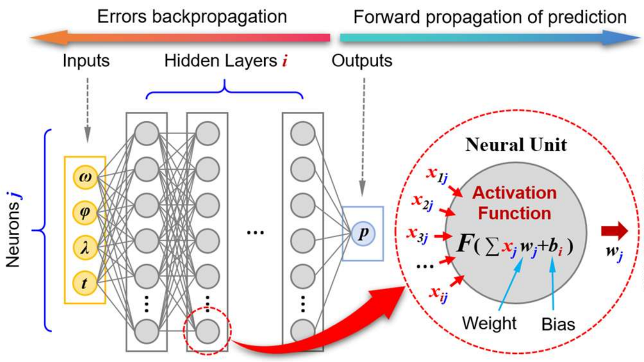

Figure9: Neural unit of the PINN model for prediction.

$$L(w,b) = L_{\text{t}} + L_{\text{cir}} + L_{\text{b}} + L_{\text{m}} \tag{22}$$

$$L_{\text{t}} = \frac{1}{N_{\text{t}}} \sum_{i=1}^{N_{\text{t}}} f_{\text{t}}^2 \tag{23}$$

$$L_{\text{cir}} = \frac{1}{N_{\text{cir}}} \sum_{i=1}^{N_{\text{cir}}} \left(u_{\text{n}}(\varphi_1) - u_{\text{n}}(\varphi_{\text{X}})\right)^2 \tag{24}$$

$$L_{\text{b}} = \frac{1}{N_{\text{t}}} \sum_{i=1}^{N_{\text{t}}} \left(u_{\text{n}} - u_{\text{t}}\right)^2 \tag{25}$$

$$L_{\text{m}} = \frac{1}{N_{\text{m}}} \sum_{i=1}^{N_{\text{m}}} \left(u_{\text{n}} - u_{\text{t}}\right)^2 \tag{26}$$

Where w and b represent the weights and biases, respectively. L_{t} denotes the residual of the theoretical physical equations, L_{cir} the circumferential periodicity error, L_{b} the pressure boundary condition error, and L_{m} the contact zone distribution error. f_{t} corresponds to the residual of the theoretical differential equations, u_{n} is the predicted value from the neural network, and u_{t} is the numerically solved value from the theoretical equations.

The architecture of PINNs is designed such that the number of neurons in the first layer matches the input variables, which include the circumferential coordinate φ, radial coordinate λ, rotational velocity ω, and operation time t. The final layer has neurons equal to the output variables: the pressure value p of the relevant domain node. The framework and training process of PINNs for solving the theoretical model equations under dynamic conditions are illustrated in fig. 10. The pressure distribution prediction can be generated by arranging the predicted nodal pressures into a matrix.

3.4 Theoretical evaluation of predictive capability

To verify the success of the network training and ensure that the results obtained by PINNs under this convergence criterion align with real physical scenarios, it is necessary to compare them with the results from the theoretical numerical model. The theoretical model of mixed lubrication is solved using an iterative method based on the configuration of difference-elliptic partial differential equations. The specific solution procedure can be referred to in Reference [8] and will not be reiterated here. The parameter settings for the PINN model in this study are listed in Table 2.

Table2: *Parameter settings for PINN model.*

Parameters	Value
No. of hidden layers	3/4/5
No. of neurons per layer	32/48/64
Boundary collocation points	1,000
Interior collocation points	8,200
Numerical solution data points	8,200
Training epochs	2,000

4 Experimental verification

This chapter systematically validates the hybrid lubrication model and PINNs framework through experimental studies. By establishing a controlled test platform and standardizing operating conditions, friction data under variable speeds and pressures are collected to train and test the neural network.

4.1 Experimental setup and preparations

The experimental setup employed in this study is a high-speed and high-pressure piston pump/tribological pair test platform [6,7], as illustrated in fig. 10. The test apparatus primarily consists of a loading cylinder, piston, and anti-rotation pin. The loading cylinder is equipped with four oil ports: (1) The loading port is connected to the upper chamber of the loading cavity to simulate the hydraulic clamping force of the port plate pair. (2) The draining port is linked to the lower chamber to replicate the casing pressure in a piston pump. (3) The inlet and outlet ports are connected to the kidney-shaped ports on the port plate friction pair, generating hydraulic separation forces. Prediction accuracy is rigorously evaluated by comparing model outputs against both numerical simulations and direct experimental measurements, ensuring the proposed method captures real-world mixed.

4.2 Wear test calibration

Wear tests were conducted on hard-soft and hard-hard material pairs. The valve plate surfaces used identical hard materials (DLC coating), while cylinder block specimens were made of HMn manganese brass or CrN-coated variants.

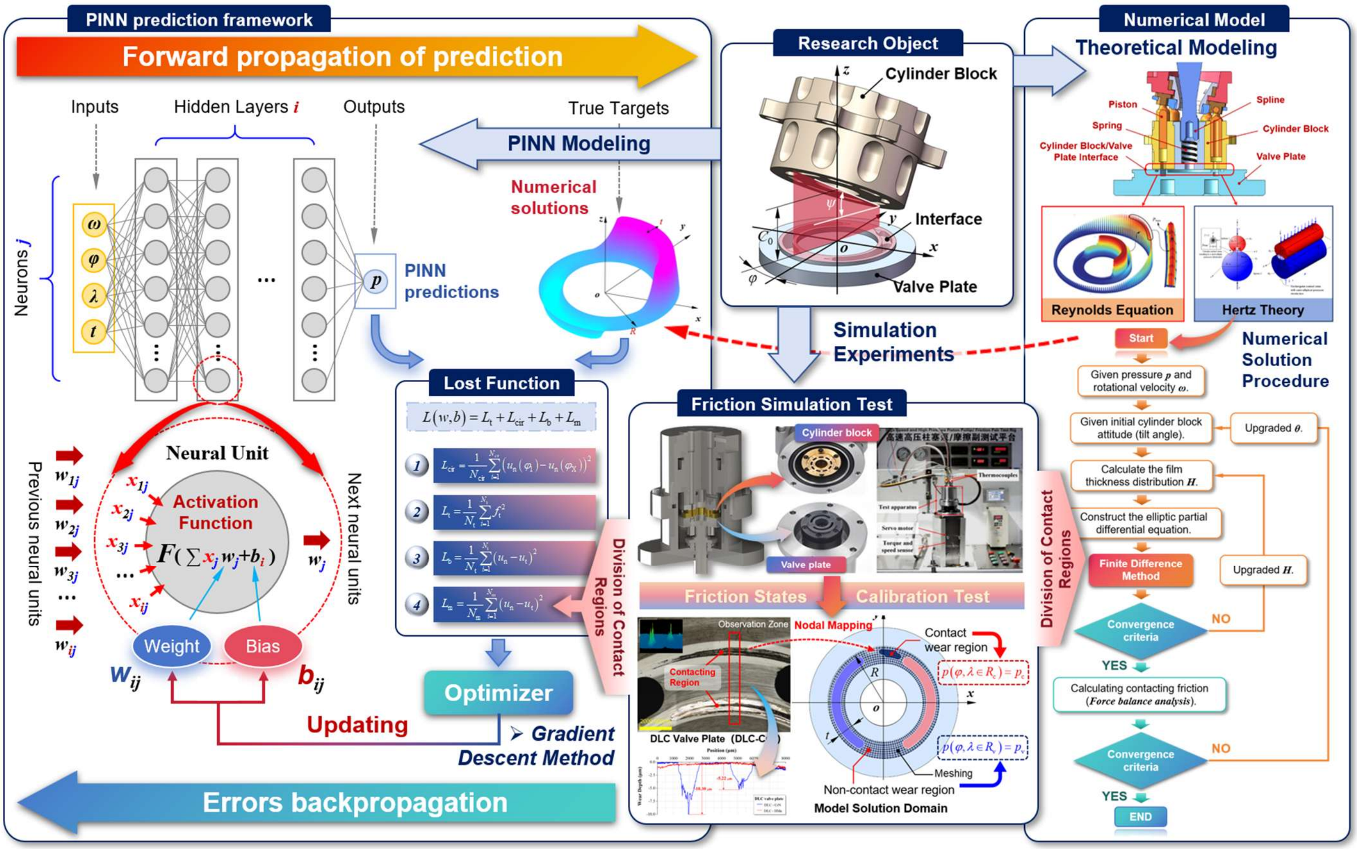

Figure10: Lubrication characteristic prediction framework with the proposed PINN model.

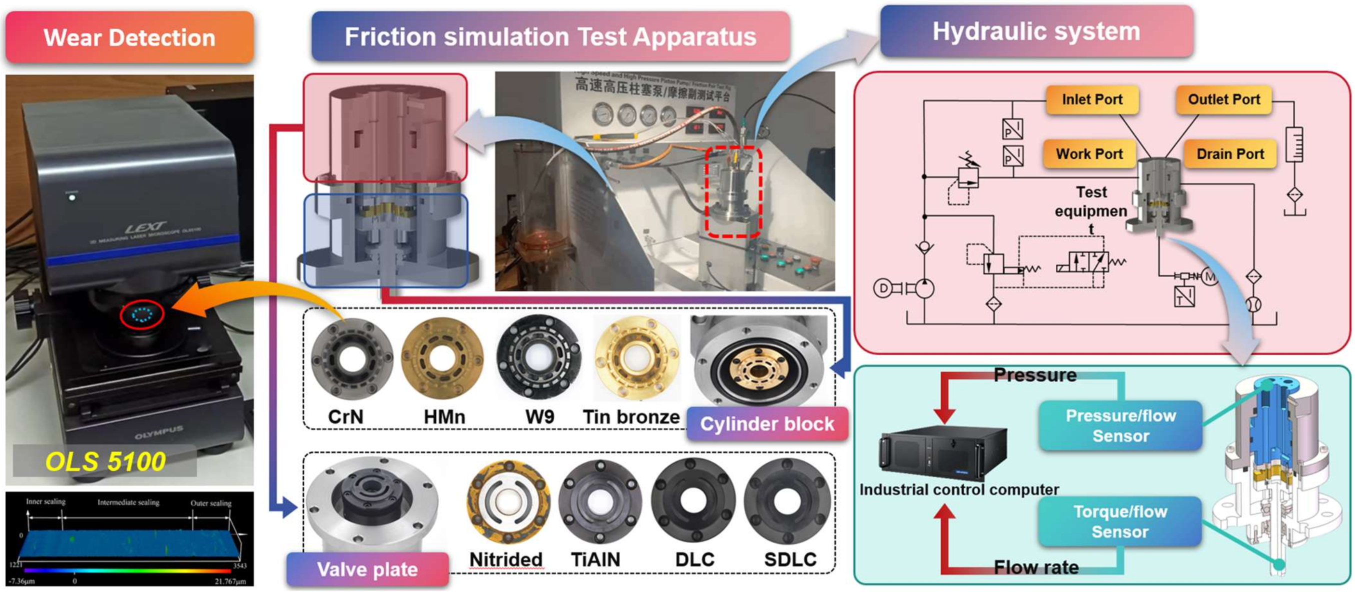

Figure11: High-speed and high-pressure piston pump/friction pair test platform.

Tests were performed under identical initial conditions (clamping force: 2.5 kN, system pressure: 7 MPa), with rotational velocity progressively increased from 0 to 10,000 rpm. Post-test analysis using a 3D laser measuring microscope (OLS5100) revealed interfacial wear patterns. Contact wear locations were identified, wear scar depths quantified, and the contact zone subset R_c was defined in the hybrid lubrication model based on measurements for experimental calibration. Fig. 12 shows concentrated wear near the dead zone, spanning 15–17% of the circumferential extent.

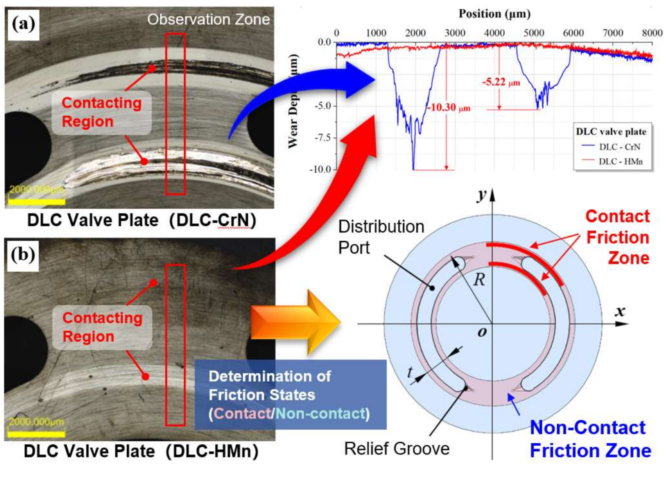

Figure*12: Determination of friction states based on experimental observation.*

Table3: *Experimental conditions (DLC-coated valve plate).*

Group	Specimens	Hardness	Conditions	Duration
1	CrN-coated	HV2200	2.5 kN/7MPa	5min
2	HMn	HV168	2.5 kN/7MPa	5min
3	CrN-coated	HV2200	3 kN/14MPa	5min
4	HMn	HV168	3 kN/14MPa	5min

4.3 Evaluation of prediction precision

By comprehensively considering the test conditions of the experimental platform, computational capabilities of the theoretical model, and lubrication/friction characterization methods, the mixed friction coefficient was selected as the observation metric. Under consistent initial operating parameters, experimental curves, numerical simulation results, and PINN-predicted curves of the mixed friction coefficient for the cylinder block/valve plate pair within the 0-10,000 rpm range were compared, as shown in fig. 13. The average error between the PINN prediction and the theoretical value is 4.132%. However, the maximum error compared to the experimental value is 17.716% due to the inherent errors in the theoretical model. Future studies should enhance PINN accuracy by increasing the incorporation of experimental measurement data (fig. 15).

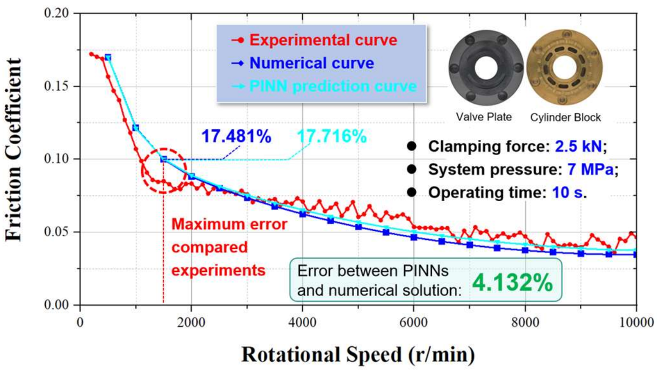

Figure13: Evaluation of predictive capability (mixed friction coefficient-speed curve).

5 Discussion

The study of lubrication under extreme conditions faces limitations in theoretical models (computational power) and experimental setups (hardware). PINNs allow efficient simulations of lubrication characteristics across extreme condition ranges.

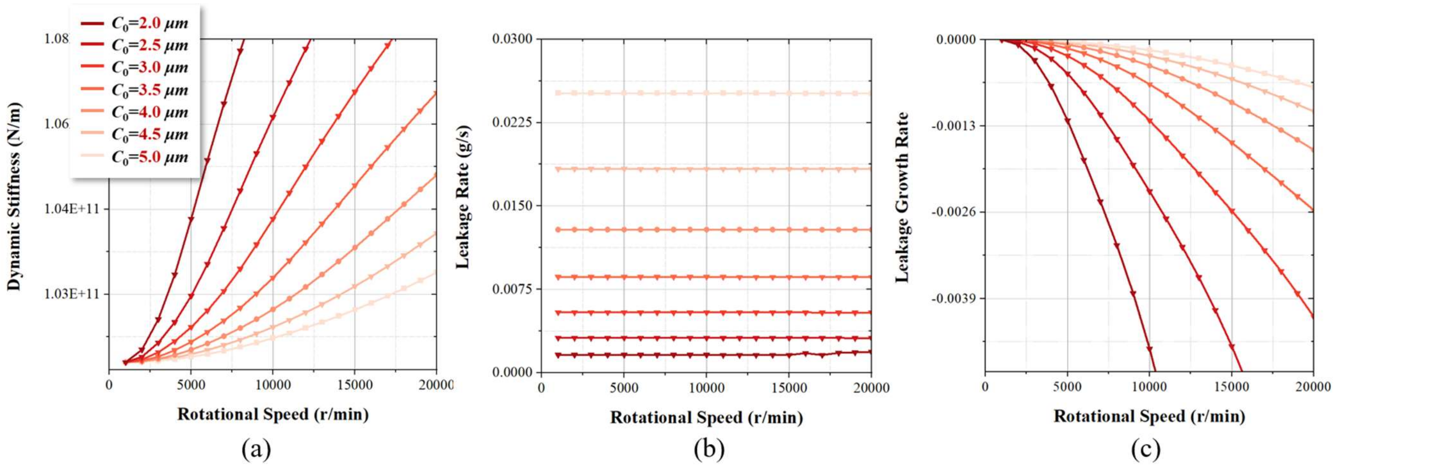

Figure14: Lubrication characteristic prediction: stiffness and internal leakage.

5.1 Dynamic lubrication analysis under extreme variable-speed condition

Lubrication characteristics were predicted over a wide speed range (0-20,000 rpm). Dynamic stiffness and internal leakage were selected as key indicators of lubrication performance and assessed at constant pressures (35 MPa load, 2 MPa system) over 10 s. As shown in fig. 14, dynamic stiffness increases monotonically with speed, while leakage decreases. Both parameters exhibit larger changes at smaller film thicknesses. Starting with an initial film thickness of 2 µm, increasing the speed by 5,000 rpm results in a 5×10^9 N/m increase in dynamic stiffness.

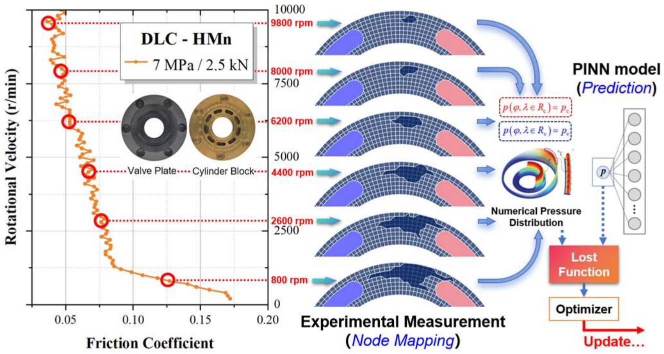

Figure15: Future perspectives: experimental calibration of variable-speed friction states.

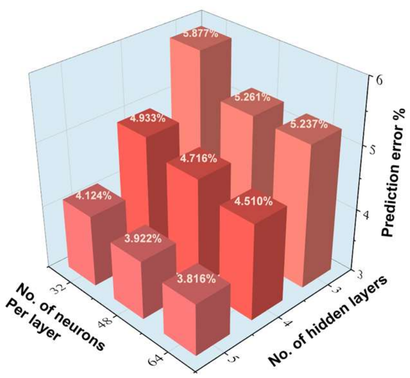

Figure16: Comparisons of prediction error.

5.2 Impact of network parameters on prediction

The impact of network depth and width on the prediction accuracy was investigated under extreme conditions (20,000 rpm, 35 MPa loading pressure, 2 MPa system pressure, 10 s duration), with 2,000 epochs of training. Results show that increasing the number of hidden layers generally led to a significant reduction in prediction errors. For instance, with 32 neurons per layer, the error decreased by 1.753% when increasing from 3 to 5 layers, compared to a 0.64% reduction when increasing neurons from 32 to 64 per layer (fig. 16). These findings suggest that network depth plays a more critical role in enhancing prediction accuracy than width, likely due to its ability to better capture the complex interactions in mixed lubrication regimes. They also highlight the need for topology-specific tuning in multi-physics applications.

6 Conclusion

This study pioneers a PINN model to decode extreme lubrication dynamics in aerospace hydraulic pumps. By synergizing Reynolds-based compressible fluid models, contact mechanics, and neural operators, the framework resolves multi-physics coupling (dynamic lubrication, asperity contact) with significant high efficiency. Validated experimentally, the PINN model achieves fast real-time analysis and <5% error in predicting mixed lubrication transitions and transient flow fields under variable speeds/pressures. This intelligent paradigm bridges first-principles physics with AI-driven modeling, offering transformative potential for next-gen pump design and condition monitoring under ultra-wide operational spectra.

Declaration of Competing Interest

The authors declare that they have no known competing financial interests or personal relationships that could have appeared to influence the work reported in this paper.

Acknowledgements

This study is supported by the Chinese national project of Electro-Hydrostatic Module and Electro-Hydrostatic Actuator.

References

[1] MARÉ J C, FU J. Review on signal-by-wire and power-by-wire actuation for more electric aircraft. *Chinese Journal of Aeronautics*, 2017, 30(3): 857-870.

[2] FU J, MARE J C, YU L, et al. Multi-level virtual prototyping of electromechanical actuation system for more electric aircraft. *Chinese Journal of Aeronautics*, 2018, 31(5): 892-913.

[3] SHOUJUN Z, JUN H, YUQIANG Z. The study on the dynamic capability of an electro-hydrostatic actuator to drive a large inertia load. In: *2016 IEEE International Conference on Aircraft Utility Systems*, 2016: 836-841.

[4] FU Y, LI Z, AN G, et al. Electrohydraulic pump development status and key technology review. *Machine Tool & Hydraulics*, 2012, 40(1): 143-149+160.

[5] ALLE N, HIREMATH S S, MAKARAM S, et al. Review on electro hydrostatic actuator for flight control. *International Journal of Fluid Power*, 2016, 17(2): 125-145.

[6] FU J, LYU D, KANG J, et al. Tribological characteristics of hard-to-hard matching materials of cylinder block/valve plate interface in electro-hydrostatic actuator pumps. *Proceedings of the Institution of Mechanical Engineers, Part C: Journal of Mechanical Engineering Science*, 2023, 237(16): 3692-3705.

[7] LYU D, FU J, CI K, et al. Experimental Research on Friction Characteristics of DLC Coated Cylinder Block/Valve Plate Interface in Aerospace Integrated Motor Pumps. In: *2023 Asia-Pacific International Symposium on Aerospace Technology Proceedings. Springer Nature*, 2024: 1141-1156.

[8] LYU D, FU J, ZHAO S, et al. Development of Boundary/Mixed Friction Models for Cylinder Block/Valve Plate Interface in a Novel Aerospace Electro-Hydrostatic Module. In: *BATH/ASME Symposium on Fluid Power and Motion Control. ASME Press*, 2024: FPMC2024-140246.

[9] ZHAO J, FU Y, MA J, et al. Review of cylinder block/valve plate interface in axial piston pumps: Theoretical models, experimental investigations, and optimal design. *Chinese Journal of Aeronautics*, 2021, 34(1): 111-134.

[10] LI J, ZHANG W, YUE J, et al. A deep learning method for incompressible fluid equations and coupled problems. Mathematica *Numerica Sinica*, 2024, 46(2): 232-252.

[11] KARKOUB M A, GAD O E, RABIE M G. Predicting axial piston pump performance using neural networks. *Mechanism and Machine Theory*, 1999, 34(8): 1211-1226.

[12] GUO J, YANG Y, LI H, et al. A parallel deep neural network for intelligent fault diagnosis of drilling pumps. *Engineering Applications of Artificial Intelligence*, 2024, 133: 108071.

[13] ROJEK M, BLACHNIK M. A Dataset and a Comparison of Classification Methods for Valve Plate Fault Prediction of Piston Pump. *Applied Sciences*, 2024, 14(16): 7183.

[14] HESS N, SHANG L. Development of a Machine Learning Model for Elastohydrodynamic Pressure Prediction in Journal Bearings. *Journal of Tribology*, 2022, 144(8): 081603.

[15] PERIC B, ENGLER M, SCHULER M, et al. Using Neural Networks as a Data-Driven Model to Predict the Behavior of External Gear Pumps. *Processes*, 2024, 12(3): 526.

[16] REN H J, YUAN X X, CHEN J Q, et al. Neural network prediction of Reynolds stress anisotropy tensor under wide-speed conditions. *Chinese Journal of Theoretical and Applied Mechanics*, 2022, 54(2): 198-212.

[17] EIVAZI H, TAHANI M, SCHLATTER P, et al. Physics-informed neural networks for solving Reynolds-averaged Navier–Stokes equations. *Physics of Fluids*, 2022, 34(7): 075117.

[18] RAMOS D J, CUNHA B Z, DANIEL G B. Evaluation of physics-informed neural networks (PINN) in the solution of the Reynolds equation. *Journal of the Brazilian Society of Mechanical Sciences and Engineering*, 2023, 45(11): 568.

[19] WANG Z, ZHOU Z, XU W, et al. Physics informed neural networks for fault severity identification of axial piston pumps. *Journal of Manufacturing Systems*, 2023, 71: 421-437.

[20] DONG C, TAO J, SUN H, et al. Innovative fault diagnosis for axial piston pumps: A physics-informed neural network framework predicting pump flow ripple. *Mechanical Systems and Signal Processing*, 2025, 225: 112274.

[21] LIU X, CHENG W, XING J, et al. Hierarchical Physics-Informed Neural Network for Rotor System Health Assessment. *IEEE Transactions on Automation Science and Engineering*, 2024, 21(3): 1-14.

[22] YIN F, LUO H, NIE S, et al. Physics-Informed machine learning for tribological properties prediction of S32750/CFRPEEK tribopair under seawater lubrication. *Tribology International*, 2024, 199: 109965.

[23] MA Z, LIAO H, GAO J, et al. Physics-Informed Machine Learning for Degradation Modeling of an Electro-Hydrostatic Actuator System. *Reliability Engineering & System Safety*, 2023, 229: 108898.